Modeling the toroidal asymmetry of heat load impacted by Nitrogen injection in EAST using EMC3-EIRENE

Yang Luo[1], Haifeng Liu[1,*], Yuhong Xu[1,*], Yuhe Feng[2], Wenfeng Guo[3], Chunfeng Dong[4], Xianqu Wang[1], Jie Huang[1], Hai Liu[1], Xin Zhang[1], Wei Li[1], Lang Yang[1], Yangbo Li[1], Jinmao Liu[1], Jun Cheng[1] and Changjian Tang[5]

[1] Institute of Fusion Science, School of Physical Science and Technology, Southwest Jiaotong University, Chengdu, 610031 China
[2] Max-Planck-Institute für Plasmaphysik, Association EURATOM-IPP, Greifswald 17491, Germany
[3] Institute of Plasma Physics, Chinese Academy of Sciences, Hefei 230031, China
[4] Southwestern Institute of Physics, PO Box 432, Chengdu 610041, People's Republic of China
[5] School of Physical Science and Technology, Sichuan University, Chengdu 610065, China

E-mail: hfliu@swjtu.edu.cn and xuyuhong@swjtu.edu.cn

Abstract: The effects of Nitrogen injection on heat load in the scape-off layer (SOL) are systematically investigated in the EAST double-null divertor configuration using EMC3-EIRENE code. Nitrogen impurities injected near the separatrix line and away from the separatrix line give rise to a non-axisymmetric distribution of heat load on the target plate. With impurity injection near the separatrix line, the occurrence of the toroidal asymmetric heat load is observed only nearby the toroidal injection location, while with the injection away from the separatrix line the regions of the asymmetric heat load extend and deviate from the toroidal injection position. The competition between the friction force and the ion temperature gradient force has been analyzed. It shows that when impurities are injected away from the separatrix line more impurities can be parallelly transported to a further toroidal location, which results in the extension and deviation of the non-symmetric electron temperature. When the input power is increased, the non-symmetric phenomenon of the heat load turns to be insignificant due to the reduction of the impurity density in the downstream regions, as illustrated by the field line tracing technique. Furthermore, by scanning various injection positions in the EAST tokamak, the optimum location of impurity injection has been discovered.

Keywords: EMC3-EIRENE simulation, SOL, gas puffing, heat deposition

1. Introduction

Impact of gas injection on the edge plasma transport is crucial to long-pulse high-performance operations in tokamaks. In order to stably control plasma conditions in experiments it is necessary to evaluate the particle and energy deposition on the tokamak target in 3D geometric configurations. The heat flux on the divertor targets is expected to decrease to an acceptable level through injecting gas like Nitrogen, Neon and Argon. Theoretical and experimental investigations have been widely carried out to reduce the heat flux on the targets and plasma wall interactions in EAST[1], JET[2-3], LHD[4] ,W7-AS[5] and ITER[6-7]. In the future, the materials of divertor plates in EAST would be upgraded to tungsten on both of up and low plates based upon the cassette and mono-block technology like ITER which could endure the heat load within the limit of 10 MW/m^2[8]. High-Z impurity like tungsten melting from the plasma facing components (PFCs)[9] can significantly damage the plasma confinement performance by means of radiative power losses and

fuel dilution, causing plasma disruptions and cooling. Hence, studies of edge impurity transport and power deposition under the condition of high input power discharge are important to deeply understand the divertor operation.

Gas injection is one of the most promising methods to keep heat flux as low levels during the long -pulse steady-state operation. The codes such as SOLPS[10-11] and EMC3-EIRENE[12-13] have been widely used to investigate the edge plasma and impurity transport in the toroidal magnetic confinement devices. EMC3-EIRENE is a parallel package for the study of three-dimensional boundary plasma and impurity transport. It uses a complex physical model containing the mass, momentum and energy equations, the collision between particles, the atomic processes, and the interaction between the plasma and the first wall. The non-axisymmetric phenomena are intrinsic in stellarators[14-16]. This code has been successfully applied to many fusion devices including W7-AS[12-17], LHD[18-21], DIII-D[22], ASDEX Upgrade[23-24] and EAST[25-27]. Recently numerical research shows that lithium emission pattern simulated by EMC3-EIRENE presents three-dimensional distribution in EAST[28-30], which are in good agreement with experiment results measured by the CCD camera. Effects of neon injection positions on heat flux distribution on EAST have been investigated numerically, which shows a lower heat load with the injection near the strike points and the symmetric distribution of heat load with the injection away from strike points[31]. However, the influence of Nitrogen injection on the toroidal asymmetric distribution of heat load on the divertor is not adequately revealed. In order to optimize impurity puffing position for heat flux mitigation, it is of great importance to investigate the heat flux distributions with different Nitrogen injected positions.

In this paper, we use EMC3-EIRENE code to simulate the edge plasma transport in EAST. In Section 2, the divertor geometry of the EAST configuration and the physical model of the EMC3-EIRENE code are addressed. The effects of Nitrogen injections on the symmetric/asymmetric heat load are studied in Section 3. Then, we focus on the influence of the momentum transport on the edge plasma temperature and illustrate the impurity density as well as radiation distribution along the magnetic field with different input powers in Section 4. Finally, conclusions are showed in the last section.

2. Computation Grid and Physical Modeling

In this study, the computational grid is constructed by the shot number #048466 of EAST double-null magnetic configuration shown in Figure 1 (a). The schematic drawing of Nitrogen impurity injection positions marked by the black circles shown in Figure 1(b). The equilibrium is provided by equilibrium fitting (EFIT) code and the toroidal magnetic field B = 1.8 T. The grid comprises six sub-zones including (1) the main plasma core region; (2) SOL region between the first and second separatrix; (3) left and (4) right SOL outward the second separatrix; (5) up and (6) down private flux regions. To obtain the particle flux from the core plasma, the simulation domain for EMC3-EIRENE is extended inside the core plasma. The radial, poloidal and toroidal resolutions of the core mesh are set as 90, 300 and 17, respectively for each toroidal segment, which has a toroidal length of 36°. Periodic boundary conditions are utilized to generate the mesh of 360° in the toroidal direction by reversible field-line mapping (RFLM) numerical technique which uses bilinear field-

line interpolation method to solve the boundary numerical problem[32-33].

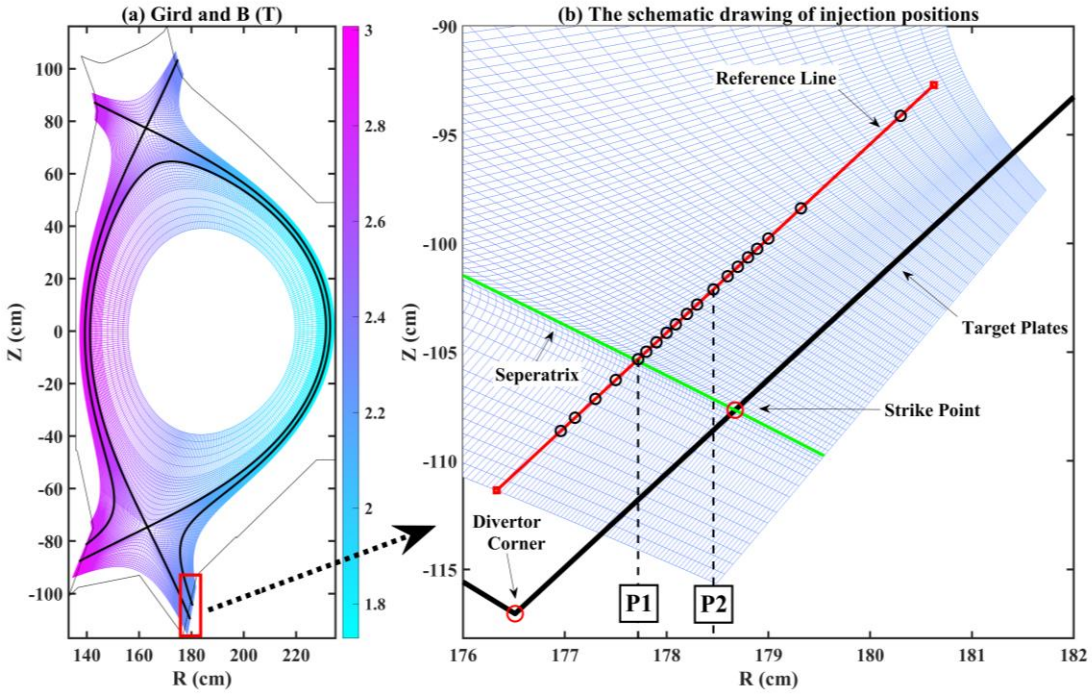

Figure 1. The poloidal cross section of the EAST double null configuration grid and the distribution of the magnetic strength (a). The schematic drawing of Nitrogen impurity injection positions (b) marked by the black circles along the red reference line. Two of them, P1 near the separatrix and P2 away from the separatrix are indicated by two black dashed vertical lines.

The EMC3-EIRENE code self-consistently combines EMC3 with EIRENE. EMC3 solves the steady-state plasma fluid equations of mass, momentum and energy in the arbitrary magnetic geometry using locally field -aligned fluid equations. EIRENE handles the neutral particle transport and the corresponding atomic and molecular processes. Besides, the transport, collision with main plasma, ionization and recombination process of the impurity are also contained into the physical model. An exponential decay is utilized at the plasma boundary. The EMC3-EIRENE formulas are as follows:

$$\nabla\cdot(n_i u_{i\|}\mathbf{e}_\| - D_\perp \ddot{\mathbf{I}}_\perp\cdot\nabla n_i) = S_p \tag{1}$$

$$\nabla\cdot(m_i n_i u_{i\|}^2\mathbf{e}_\| - \eta_\|\mathbf{e}_\|\mathbf{e}_\|\cdot\nabla u_{i\|} - D_\perp \ddot{\mathbf{I}}_\perp\cdot\nabla m_i n_i u_{i\|}) = -\mathbf{e}_\|\cdot\nabla p + S_m \tag{2}$$

$$\nabla\cdot\left[\frac{5}{2}T_i\left(n_i u_{i\|}\mathbf{e}_\| - D_\perp\ddot{\mathbf{I}}_\perp\cdot\nabla n_i\right) - \left(\kappa_{i\|}\mathbf{e}_\|\mathbf{e}_\| + \chi_{i\perp}n_i\ddot{\mathbf{I}}_\perp\right)\cdot\nabla T_i\right] = \frac{3m_e n_e}{m_i\tau_{ei}}(T_e - T_i) + S_{ei} \tag{3}$$

$$\nabla\cdot\left[\frac{5}{2}T_e\left(n_e u_{i\|}\mathbf{e}_\| - D_\perp\ddot{\mathbf{I}}_\perp\cdot\nabla n_e\right) - \left(\kappa_{e\|}\mathbf{e}_\|\mathbf{e}_\| + \chi_{e\perp}n_e\ddot{\mathbf{I}}_\perp\right)\cdot\nabla T_e\right] = \frac{3m_e n_e}{m_i\tau_{ei}}(T_i - T_e) + S_{ee} + S_{e,cool} \tag{4}$$

Here, Eqs. (1) - (4) represent the particle balance, momentum balance ions and electrons energy balance, respectively. S_p, S_m, S_{ee}, S_{ei} represent the particle, momentum, electron and ion energy sources from neutrals. $S_{e,cool}$ is the energy loss due to radiation and ionization and $Q = 3m_e n_e (T_e - T_i)/m_i \tau_{ei}$ is energy loss due to ion and electron collisions. $\mathbf{e}_{\|}$ is the unit vector along the magnetic field and $\ddot{\mathbf{I}}_{\perp}$ is the perpendicular unit tensor. $D_{\perp}$, $\chi_{e\perp}$, $\chi_{i\perp}$, $\kappa_{e\|}$ and $\kappa_{i\|}$ are the cross-field diffusion coefficients, cross-field electron energy transport, cross-field ion energy transport, electron parallel thermal conductivity and ion parallel thermal conductivity coefficients , respectively. Plasma are considered to transport from the upstream region to the target plates at the thermal speed. It is assumed that plasma ions and electrons are completely neutralized on the targets and the flux of neutral particles are considered at the plates. Despite the absence of effects of volume recombination and flux limiters , simulation results from EMC3-EIRENE are in good agreement with these from SOLPS[34]. Due to numerical difficulties, the implementation of drift effects in the 3D model is a matter of ongoing development[35]. In terms of the impurity edge transport, it contains classic transport along the magnetic field line and diffusion perpendicular to the parallel direction. The parallel forces on impurity ions are friction force, impurities pressure gradient, electrical force, electron temperature gradient force and ion temperature gradient force:

$$\nabla \cdot (n_I^z V_{I\|}^z \mathbf{e}_{\|} - D_I^z \ddot{\mathbf{I}}_{\perp} \cdot \nabla n_I^z) = S_{z-1\to z} - S_{z\to z+1} + R_{z+1\to z} - R_{z\to z-1} \tag{5}$$

$$U_{Ii}^z (V_{I\|}^z - V_{i\|}^z) = -\mathbf{e}_{\|} \cdot \nabla n_I^z T_I^z + n_I^z ZeE_{\|} + n_I^z Z^2 \alpha_{Ie} \mathbf{e}_{\|} \cdot \nabla T_e + n_I^z \alpha_{Ii} \mathbf{e}_{\|} \cdot \nabla T_i \tag{6}$$

Where $S_{z-1\to z} - S_{z\to z+1} + R_{z+1\to z} - R_{z\to z-1}$ are the ionization and recombination rates for impurities, the subscript I and z represent the impurity and the charge number, the friction coefficient $U_{Ii}^z = m_z n_I^Z / \tau$, τ is the mean impurity-ion collision time, the parameters α_{Ie} and α_{Ii} are the coefficients of the temperature gradient force, the cross-field diffusion coefficient of impurity is D_I^z and the impurity temperature equal the plasma ion temperature $T_I^z = T_i$.

Figures 2 (a) - (c) show the poloidal cross-sections of electron density, electron temperature and ion temperature with the input power $P_{in} = 1\,\mathrm{MW}$ and the upstream electron density $\mathrm{n_e} = 1.0\times10^{19}\mathrm{m}^{-3}$. Input power in SOL regions is the summation of heat power and radiation loss power from the core plasma. Figures 2(d) - (f) show the electron density, electron temperature and ion temperature profiles at the outer-mid plane, respectively. The cross-field transport coefficients are established by fitting the upstream density and temperature profiles, which are considered as typical empirical parameters $D_{\perp} = 0.3\ m^2 \cdot s^{-1}$ and $\chi_{i\perp} = \chi_{e\perp} = 1.0\ m^2 \cdot s^{-1}$.

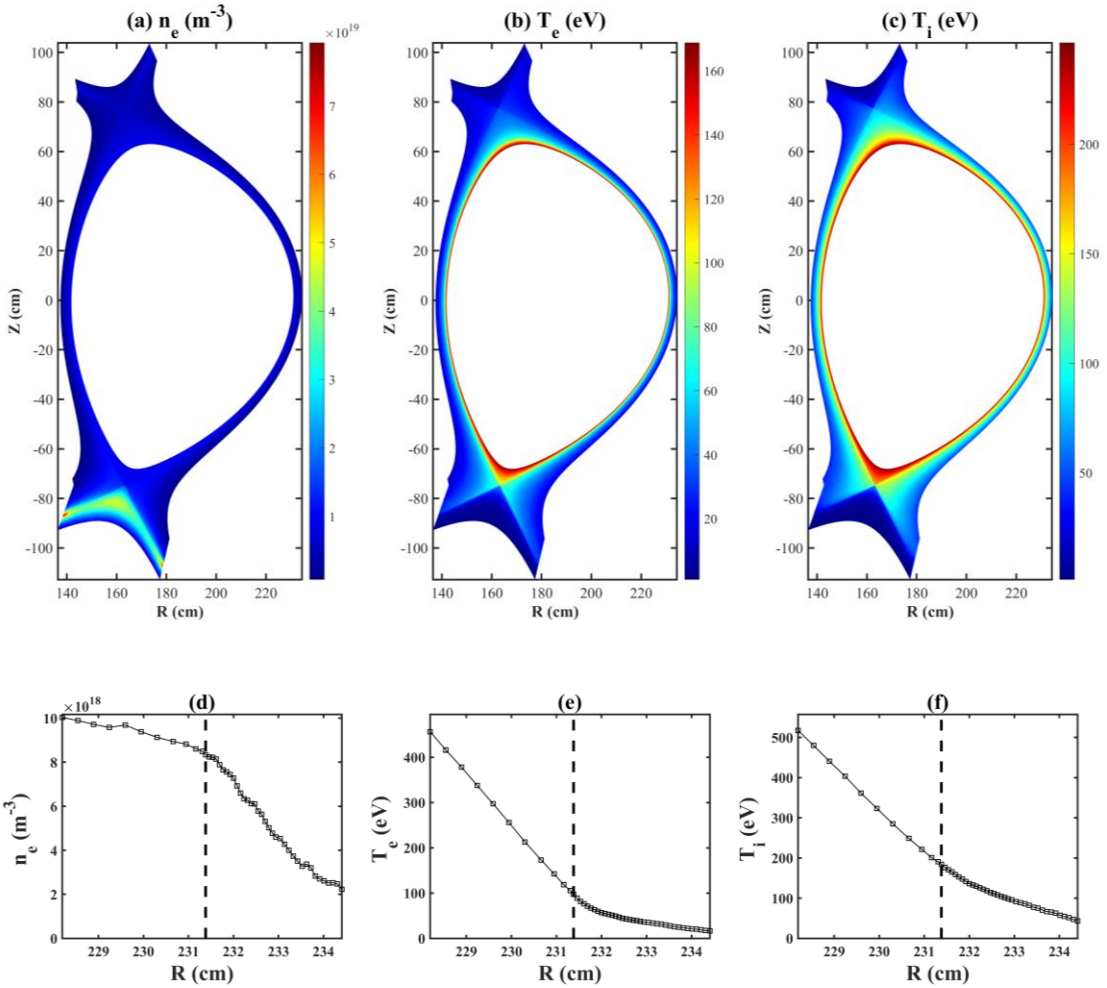

Figure 2. The poloidal cross-sections of electron density (a), electron temperature (b) and ion temperature (c) at the toroidal angle $\varphi = 0^0$; The radial profiles of plasma density (d), electron temperature (e) and ion temperature (f) at the outer-mid plane. The dashed lines correspond to the last close flux surface.

In simulations, we scan the input power P_{in} from 1 MW to 6 MW with keeping other initial parameters as constants. Figure 3 show the distribution of heat flux at the out-lower target plates without the impurity. The x-axis desribes the distance to the divertor corner on the target plates. The positions of peak values are close to the strike point on the target plates. The peak values of heat load increase from $1.0\ \mathrm{MW/m^{-2}}$ to $14.5\ \mathrm{MW/m^2}$ .The heat flux can be evaluated by the two-point model on the edge transport in SOL, which illustrates the particle and energy transport between the upstream regions and the downstream regions. The assumption, $T_t^{7/2} \ll T_u^{7/2}$ and $q_{\parallel} \approx P_{in} / A_{\parallel}$, is under consideration. The term $A_{\parallel}$ denotes the total cross-sectional area of the SOL for power flow. Therefore, the downstream temperautre and density of two-point model could be analytically solved as the target temperature $T_t = 2m_i q_{\parallel}^2 \left(7q_{\parallel}L/2\kappa_{0e}\right)^{-\frac{4}{7}} \Big/ \left|e^3\right| \gamma^2 n_u^2$ and the target density $n_t = \gamma^2 \left|e^2\right| n_u^3 \left(7q_{\parallel}L/2\kappa_{0e}\right)^{\frac{7}{6}} \Big/ 4m_i q_{\parallel}^2$. The maxmum vaule of heat flux $q_t = \gamma n_t k T_t c_{st}$ grows exponentially with increasing input power.

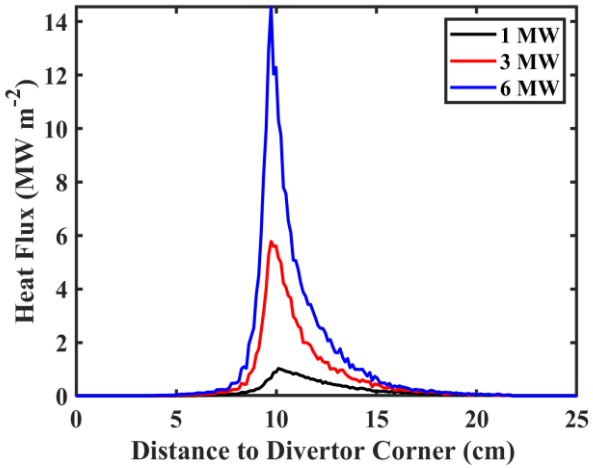

Figure 3. The distributions of heat flux on the outer-lower divertor plates for the different input power 1 MW, 3 MW and 6 MW. The x-axis represents the distance to the divertor corner.

3. Non-symmetric heat flux

In this section, the effect of the Nitrogen impurity injection on the heat load at divertor targets has been investigated. The impurities are injected near the separatrix P1 and away from the separatrix P2 indicated by black dashed lines in Figure 1 (b). The impurity diffusion coefficient is $D_I = 0.5\ m^2 \cdot s^{-1}$. Based on the seeding rate of the gas puffing system in EAST, the injection flux (the total number of impurity particles per second) is set as $6.24 \times 10^{20} s^{-1}$ with the initial impurity energy of 0.03 eV[31]. Figure 4 shows the toroidal distribution of heat flux on the out-lower divertor plates with Nitrogen impurity seeding at P1 (a, c, e))/P2 (b, d, f) and the input power are 1 MW (a, b), 3 MW (c, d) and 6 MW (e, f), respectively. The vertical axis represents the distance to the divertor corner. The dashed lines correspond to the toroidal injected position at the same toroidal angle $\varphi = 0^0$. With the impurity injection at P1 and the low input power (1MW), the heat load significantly decreases near the injection position (from $\varphi = 0^0$ to $\varphi = -36^0$) in Figure 4 (a). A significant impurity radiation near the toroidal injected position leads to a non-symmetric distribution of heat load. It is noteworthy that with the impurity injection at P2, the symmetry-breaking phenomenon extends from $\varphi = 0^0$ to $\varphi = -72^0$ in Figure 4 (b). As the input power increases, such a non-symmetric structure disappears shown in Figures 4 (e) and (d, f). Detailed analysis has been given in the following subsections.

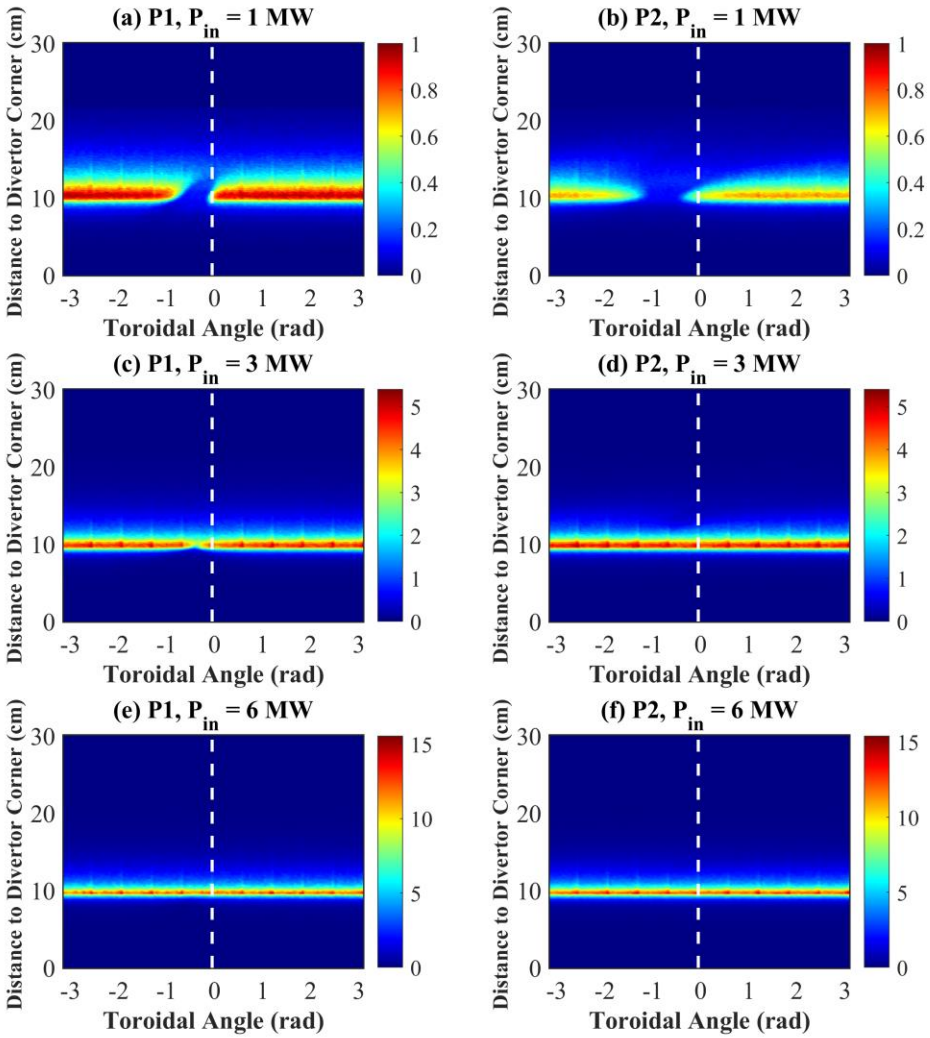

Figure 4. The distributions of heat flux on the out-lower divertor plates with Nitrogen injected near the separatrix (a, c, e) and away from the separatrix (b, d, f). The input powers are 1 MW (a, b), 3 MW (c, d) and 6 MW (e, f), respectively. The dashed lines correspond to the toroidal injected position at the same toroidal angle $\varphi = 0^0$. The horizontal axis and vertical axis are the toroidal angle and the distance to the divertor corner, respectively.

To adequately investigate the above-mentioned asymmetric heat load, the radial distributions of the momentum (a) the electron temperature (b), the Nitrogen density (c) and the radiation power (d) along the reference line with Nitrogen injected at P1 (1 MW) and P2 (1 MW) shown in Figures 5 and 6, respectively. The five curve lines illustrate different toroidal angles located at $\varphi = 0^\circ$ (black), $\varphi = -18^\circ$ (blue), $\varphi = -36^\circ$ (red), $\varphi = -54^\circ$ (green) and $\varphi = -72^\circ$ (purple). The parallel momentum transport of impurities is mainly dominant by the friction force and ion temperature gradient force along the magnetic field shown in the Eq. (6), while the radial penetration depth of the Nitrogen impurity is a complex physical process, which is determined by both the cross-field diffusion coefficient and the ionization process. The absolute difference of the momentum driven by the friction force and the temperature gradient force is displayed in Figures 5 (a) and 6 (a), where

the red dashed lines correspond to the radial injected positions. When the friction force is dominant (R ≈ 176.8 ~ 178.0 cm), the force is to push the impurity to the divertor targets along the magnetic line which leads to enhancement of the impurity density and the radiation power on the targets shown in Figure 5 (c, d) and 6 (c, d). On the contrary, if the ion temperature gradient force is dominant (R ≈ 178.0 ~ 179.0 cm), the impurity is transported to the upstream regions, giving rise to a decrease of the impurity density and the radiation power. It can be seen that the higher ion temperature gradient force leads to the lower impurity density at P1 (R ≈ 178.0 ~ 179.0 cm) compared that at P2 in Figures 5 (a) and 6 (a). A correlation of an increase of the impurity radiation with a decrease of the temperature is observed in Figures 5 (b, d) and 6 (b, d). It is noted that around the toroidal angle $\varphi = 0^0$ the peak electron temperature is greatly decreased in Figure 5 (b). However, the toroidal region with decreased peak electron temperature extends from $\varphi = 0^0$ to $\varphi = -72^0$ as shown in Figure 6 (b). Therefore, more impurities can be parallelly transported to a further toroidal region by the friction force combined with the lower ion temperature gradient force when impurities are injected away from the separatrix, which broadens the non-axisymmetry of electron temperature. Thus, in Figure 4 (b) a significant extension and deviation of the regions of reduced heat load around the injection point are found.

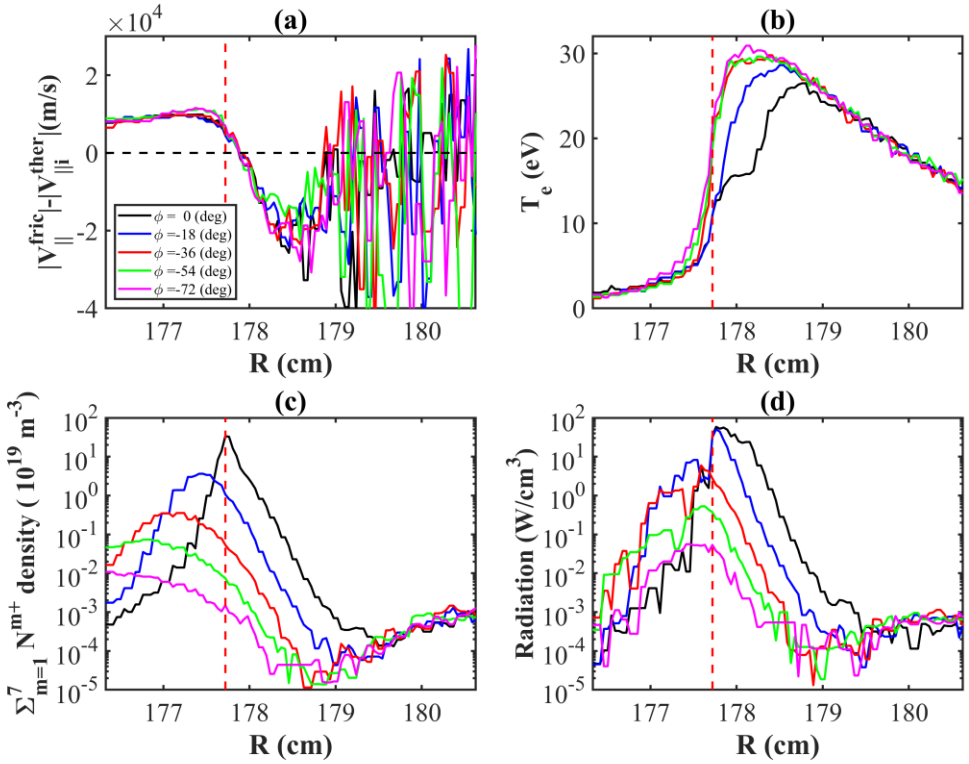

Figure 5. The radial profiles of the absolute difference of the momentum driven by the friction force and the temperature gradient force (a), electron temperature (b), Nitrogen ion density (c) and radiation power (d) at the toroidal angle from $\varphi = 0^\circ$ to $\varphi = -72^\circ$ with the impurity injected at P1 (1 MW), respectively. The red dashed lines describes the radial position of P1.

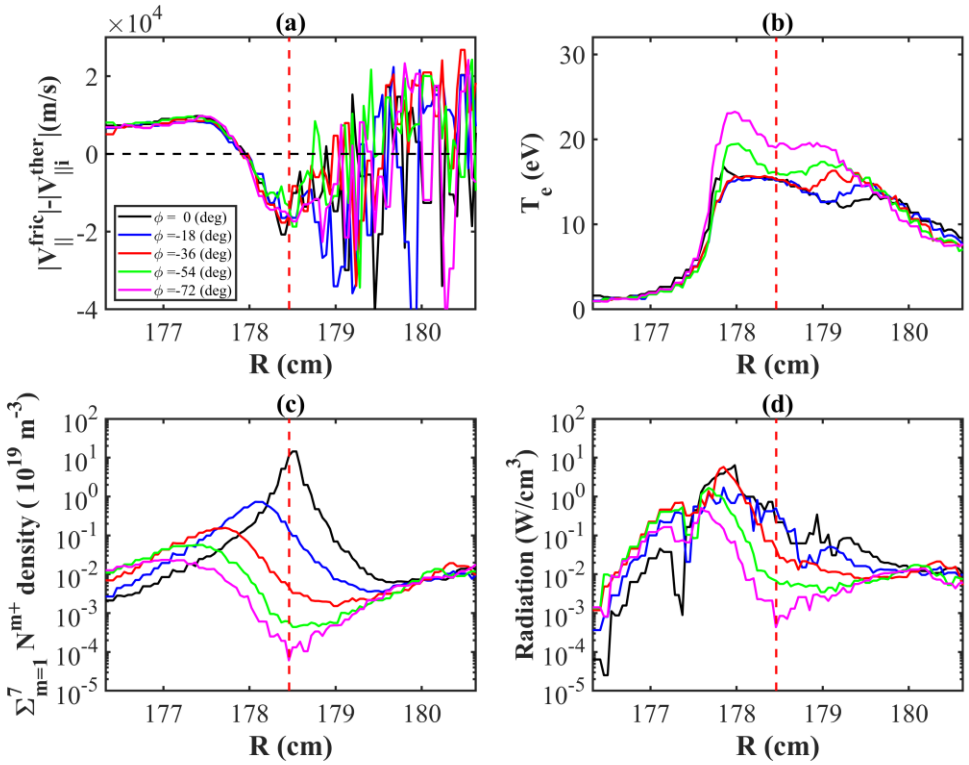

Figure 6. The radial profiles of the absolute difference of the momentum driven by the friction force and the temperature gradient force (a), electron temperature (b), Nitrogen ion density (c) and radiation power (d) at the toroidal angle from $\varphi = 0^\circ$ to $\varphi = -72^\circ$ with the impurity injected at P2 (1 MW), respectively. The red dashed lines describes the radial position of P2.

In order to investigate the relation between 3D Nitrogen radiation and heat flux, the field line tracing (FLT) technology is utilized. Figures 7 and 8 demonstrate the distributions of electron density (a), electron temperature (b), Nitrogen ion density (c) and radiation power (d) along the flux tube from out-lower targets to inner-lower targets with Nitrogen injected at P1 and P2, respectively. The black, red and blue solid curves represent the above-mentioned parameters with the input power equal to 1MW, 3 MW and 6MW, respectively. The start points for FLT are located on the outboard targets at toroidal angles $\varphi = 0^0$ in Figure 7 and $\varphi = -36^0$ in Figure 8. It can be seen that the downstream plasma density decreases and the amplitude of upstream temperature enhances as the input power increases shown in Figures 7 (a, b) and 8 (a, b). The impurity density and radiation with different input powers approximagtely keep simliar magnitudes on the targets plotted in Figure 7 (c,d). Moreover, the impurity density and radiation power raise with an increase of the input power at both of upstream and downstream regions. Thus, the non-symmetric heat load becomes weak with increasing the input power due to the fallen proportion between the radiation power and the total power in Figure 4 (a, c, e). The similar variation trend of Nitrogen density and radiation is observed as well at the upstream regions in Figure 8 (c, d). However, the impurity density and radiation power are negatively correlated to the input power in the downstream regions. It can be found that the radiation power for 1 MW is about three orders of magnitude higher than that for 6 MW on the targets. Therefore, the decreasing of the impurity density in the downstream regions give rise to the vanishing of non-symmetric heat load as shown in Figure 4 (b, d, f).

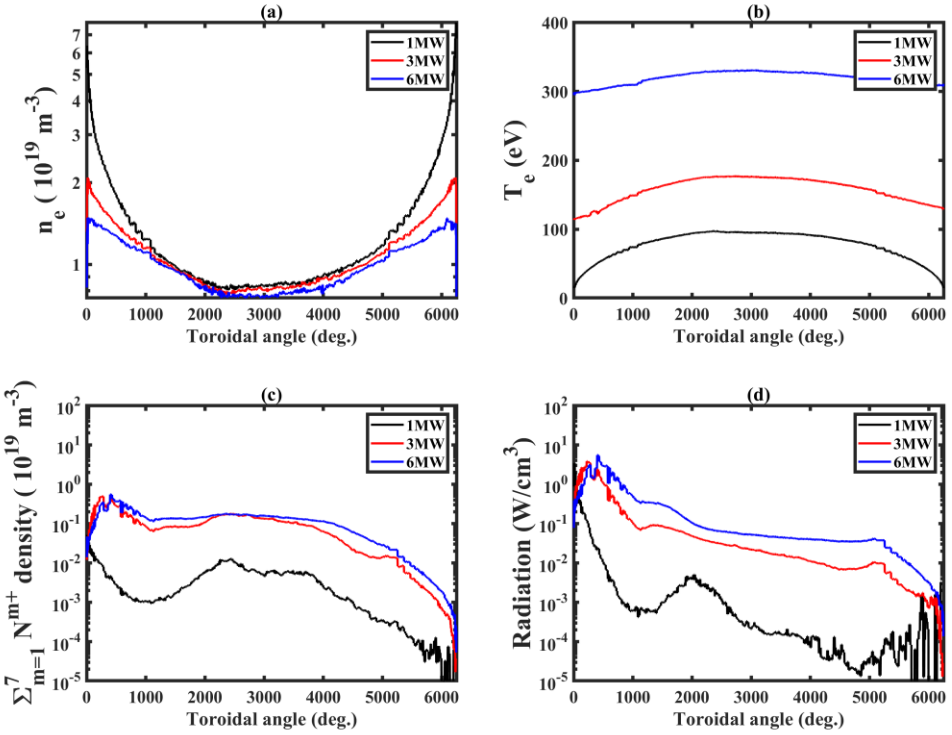

Figure 7. The electron density (a), electron temperature (b), Nitrogen ion density(c) and radiation power (d) along the magnetic field line at position P1. The black, red and blue solid curves represent the relevant distributions against the toroidal angle with the input power equal to 1MW, 3 MW and 6MW, respectively.

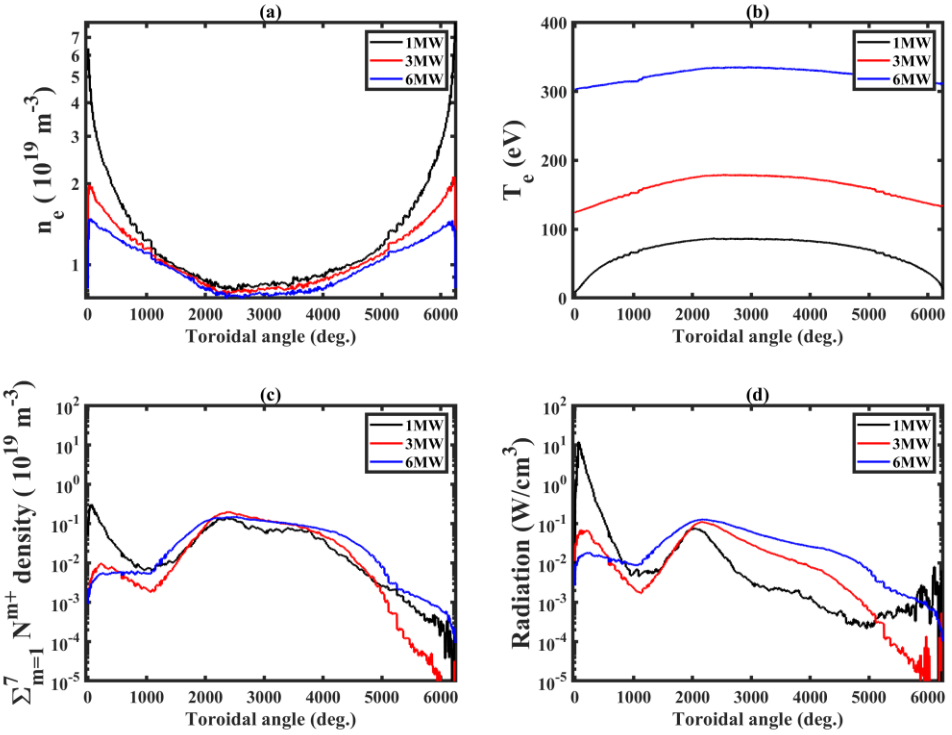

Figure 8. The electron density (a), electron temperature (b), Nitrogen ion density(c) and radiation power (d) along the magnetic field line at position P2. The black, red and blue solid curves represent the relevant distributions against the toroidal angle with the input power equal to 1MW, 3 MW and 6MW, respectively.

Additionally, a study on effects of radial impurity injected positions on heat load has been performed in Figure 9 (a, b). The injected positions scanned in the radial direction are marked by the black circles in Figure 1 (b). The horizontal axis denotes the corresponding injected positions in Figure 9. The vertical axis represents the toroidal width $\Delta\varphi$ of the non-axisymmetric heat load in Figure 9(a). In these regions the peak heat load is less than half of the maximum heat load on the global divertor plates. The $\Delta\varphi$ could quantitatively describe the non-axisymmetric phenomenon in Figure 4. The toroidal averaged peak heat load normalized by that without the impurities injected is expressed as $\alpha = \int q_{tar,peak} d\varphi / \left(2\pi q_{tar,no\ imp}\right)$ in Figure 9 (b), by which the global mitigation of heat load can be estimated. The red dashed line describes the radial position of the intersection point between the reference line and the separatrix. It is seen that the $\Delta\varphi$ rises and then declines with the radial impurity injected position in Figure 9(a) while the α descends and ascends in Figure 9(b). When the impurities are injected around R=178.15 cm, the $\Delta\varphi$ is the most significant and the α approaches to the minimum values. Hence, the impurities injected positions are located at such regions are optimal in this study.

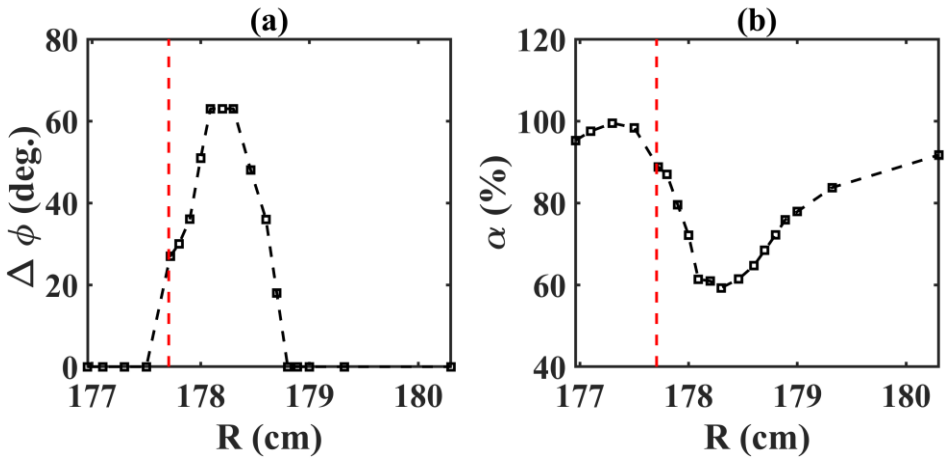

Figure 9. The toroidal width $\Delta\varphi$ of the non-axisymmetric heat load (a), the toroidal averaged peak heat load normalized by that without the impurities injected α (b) via scanning the radial injected positions with the input power 1MW. The red dashed line describes the radial position of the intersection point between the reference line and the separatrix.

4. Summary

Based on the EMC3-EIRENE modeling, an analysis of the non-axisymmetric heat flux deposition induced by Nitrogen impurity has been performed in the EAST configuration. The simulation results demonstrate that: The heat load decreases locally with the Nitrogen injection due to the impurity

radiation. It is found that Nitrogen injected at point P1 leads to toroidal asymmetric heat deposition near the toroidal injection position on the target plates. However, this asymmetric structure extends and deviates from the toroidal injection position with the impurities injected at P2. The reason is that the friction force combined with the lower ion temperature gradient force parallelly drives more Nitrogen impurities to the targets, which leads the region with decreased electron temperature to broaden. Furthermore, by the field line tracing technique, the transport of Nitrogen along the flux tube is investigated to reveal that the decreasing of the impurity density in the downstream regions result in the disappearing of non-symmetric heat load as the input power increases. In addition, when the impurity injected positions are displaced from the separatrix, the global heat load is significantly mitigated with a wide non-axisymmetric structure.

Acknowledgments

We would like to thank Shuyu Dai, Tian Xie and Juan Huang for fruitful discussions. This work was partly supported by the National Key R&D Program of China under Grant Nos. 2017YFE0301705 and 2017YFE0300402, the National Natural Science Foundation of China under Grant No. 11820101004, the Advanced Foreign Expert Introduction Program under Grant No. G20200023025 and the Fundamental Research Fund for the Central Universities under Grant No. 2682020ZT111.

Reference

[1] Chen J B *et al* 2017 *Chin. Phys. B* **26** 095205
[2] Oberkofler M *et al* 2013 *J. Nucl. Mater.* **438** S258-S261
[3] Huang J *et al* 2019 *Plasma Phys. Control. Fusion* **61** 025018
[4] Tanaka H *et al* 2017 *Nucl. Mater. Energy* **12** 241-246
[5] Feng Y *et al* 2002 *Plasma Phys. Control. Fusion* **44** 611-625
[6] Zhang W *et al* 2019 *Nucl. Mater. Energy* **19** 364-371
[7] Feng Y *et al* 2011 *38th EPS Conference on Plasma Physics* P1.071
[8] Xu H *et al* 2018 *IEEE Transactions on Plasma Science* **46** 1412-1416
[9] Federici G *et al* 2001 *Nucl. Fusion* **41** 1967
[10] Liu X *et al* 2016 *Fusion Eng. Des.* **112** 557-562
[11] Sang C F *et al* 2020 *Nucl. Fusion* **60** 056011
[12] Feng Y *et al* 2000 *Contrib. Plasma Phys.* **40** 271-275
[13] Feng Y *et al* 2017 *Plasma Phys. Control. Fusion* **59** 034006
[14] Xu Y 2016 *Matter Radiat. at Extremes* **1** 192-200
[15] Liu H *et al* 2021 *Nucl. Fusion* **61** 016014
[16] Wang X 2021 *Nucl. Fusion* **61** 036021
[17] Feng Y *et al* 2006 *Nucl. Fusion* **46** 807-819
[18] Dai S Y *et al* 2017 *Plasma Phys. Control. Fusion* **59** 085013
[19] Dai S Y *et al* 2016 *Contrib. Plasma Phys.* **56** 628-633
[20] Dai S Y *et al* 2016 *Nucl. Fusion* **56** 066005
[21] Dai S Y *et al* 2017 *Fusion Eng. Des.* **125** 625-630
[22] Lore J D *et al* 2017 *Nucl. Fusion* **57** 056025
[23] Brida D *et al* 2017 *Nucl. Fusion* **57** 116006
[24] Lunt T *et al* 2017 *Nucl. Mater. Energy* **12** 1037-1042

[25] Huang J *et al* 2014 *Plasma Phys. Control. Fusion* **56** 075023
[26] Xu S *et al* 2018 *Nucl. Fusion* **58** 106008
[27] Dai S Y *et al* 2020 *J. Plasma Phys.* **86** 815860303
[28] Xie T *et al* 2019 *Plasma Phys. Control. Fusion* **61** 115006
[29] Xie T *et al* 2018 *Fusion Eng. Des.* **136** 699-705
[30] Xie T *et al* 2018 *Nucl. Fusion* **58** 106017
[31] Liu B *et al* 2020 *Plasma Phys. Control. Fusion* **62** 035003
[32] Feng Y *et al* 2005 *Phys. Plasmas* **12** 052505
[33] Frerichs H *et al* 2010 *Comput. Phys. Commun.* **181** 61-70
[34] Frerichs H *et al* 2019 *Nucl. Mater. Energy* **18** 62-66
[35] Effenberg F *et al* 2019 *Nucl. Mater. Energy* **18** 262-267